communications materials

Article

https://doi.org/10.1038/s43246-024-00483-7

Candidate spin-liquid ground state in $CsNdSe_2$ with an effective spin-1/2 triangular lattice

Jie Xing[1], Sai Mu[1], Eun Sang Choi[2] & Rongying Jin[1]

Rare-earth-based triangular lattice materials are extremely attractive for studying unconventional magnetism. Here, we report the magnetic properties of layered $CsNdSe_2$ based on direct current (DC) and alternating current (AC) susceptibility measurements down to 0.04 K. While the AC susceptibility at the zero DC field shows a broad hump below 0.5 K, there is no sign of any long-range magnetic ordering. Quantitative analysis of the DC magnetic susceptibility gives the negative Curie-Weiss (CW) temperature $\theta_{CW} < 0$ in all directions, indicating antiferromagnetic interaction between Nd ions. Of particular interest is the low temperature magnetic susceptibility, which reflects the effective spin-1/2 state with $\theta^{a}_{cw}/\theta^{c}_{cw} > 3$. The estimated exchange interactions are $J_a/k_B = 1.42$ K (in-plane) and $J_c/k_B = 0.44$ K (out-of-plane), pointing to the anisotropic magnetism. First-principles calculations that include spin-orbit coupling and Coulomb correlations reveal multiple states with zero net magnetization for $CsNdSe_2$. Both experiment and simulation strongly suggest $CsNdSe_2$ has the spin liquid ground state with effective spin-1/2. Application of a magnetic field can induce long-range antiferromagnetic ordering with the maximum transition temperature around 0.3 K, in further support of the zero-field spin liquid state.

The two-dimensional (2D) triangular-lattice systems with antiferromagnetic interaction have been extremely attractive for exploring exotic ground states. One of the frontier research topics is the quantum spin-liquid (QSL) state initially proposed by Anderson[1]. In this framework, the effective spin is 1/2, so that the spin can be treated as a fermion[1–3]. Despite extensive theoretical investigation[3] and great potential for applications[4,5], experimental progress has been slow. To date, the most promising candidates are organic materials[6,7]. While a few inorganic materials have been investigated including $TbInO_3$[8], $Sr_2Cu(Te_{0.5}W_{0.5})O_6$[9], $Lu_2Mo_2O_5N_2$[10], and Cs_2CuCl_4[11], none of these cases is settled.

In the search for new QSL candidates, rare-earth (RE)-based triangular lattice materials have recently attracted wide attention. Due to the strong spin–orbit coupling (SOC) and crystal electric field (CEF) effect, the low-temperature magnetic properties of rare-earth-based magnets can be described by an effective spin-1/2 state with strong quantum fluctuations[12,13]. For example, $YbMgGaO_4$ is considered a QSL candidate[14–17], where Yb^{3+} ($4f^{13}$) with the angular momentum $J = 7/2$ at high temperatures forms an effective spin-1/2 state at low temperatures under the combination of SOC and CEF. However, the mixed sites for Mg and Ga in $YbMgGaO_4$ could perturb the system leading to another disordered state other than the QSL state[18]. Recently, the $AYbCh_2$ (A = Li, Na, K, Rb, Cs; Ch = O, S, Se, Te) family has been investigated for the possible QSL behavior[19–23]. Compared to $YbMgGaO_4$, $AYbCh_2$ provides a homogeneous environment for the Yb triangle lattice without mixed sites. The effective spin-1/2 state of $AYbCh_2$ has been confirmed based on multiple experimental methods, such as electron spin resonance, magnetization, and neutron scattering measurements[24–31]. The lack of long-range ordering (LRO) down to millikelvin implies the QSL state[19,22,31–36]. The continuum of magnetic excitation is found in $NaYbSe_2$ in inelastic neutron scattering (INS) measurement, suggesting the ground state of $NaYbSe_2$ is a QSL with a spinon Fermi surface[37]. Recently inelastic neutron scattering results have revealed a slightly weak next nearest neighbor (NNN) coupling in $AYbSe_2$ (A = K and Cs) and the ground state is located near the boundary between the 120° magnetically ordered state and QSL state[38,39].

In fact, replacing Yb with other rare-earth elements can give rise to long-range antiferromagnetic ordering as observed in $KCeS_2$[20,40–42] and $KErCh_2$[43,44]. These indicate that the realization of the QSL state requires delicate atomic arrangement in addition to spin-1/2. This includes RE-RE

[1]SmartState Center for Experimental Nanoscale Physics, Department of Physics and Astronomy, University of South Carolina, Columbia, SC 29208, USA. [2]National High Magnetic Field Laboratory, Florida State University, Tallahassee, FL 32310, USA. e-mail: rjin@mailbox.sc.edu

distance within the layer and between layers. Compared to Yb-based compounds, Nd-based $ANdCh_2$ (A = Na, K, Rb, Cs; Ch = O, S, Se, Te) has a larger intralayer and interlayer Nd-Nd distance due to larger Nd ion size, thus changing the magnetic interactions. In this article, we report the magnetic properties of $CsNdSe_2$ measured by DC and AC magnetic susceptibilities down to 0.04 K. Our results demonstrate that $CsNdSe_2$ is an excellent candidate for studying QSL physics. Although Nd^{3+} ($4f^3$) has a large angular momentum $J = 9/2$ at high temperatures, an effective spin-1/2 state with AFM interactions is obtained at low temperatures (due to strong SOC and CEF). While the AC susceptibility shows a broad hump below 0.5 K due to quantum fluctuations, there is no sign of long-range ordering down to 0.04 K. First-principles calculations are performed with the inclusion of the spin–orbit coupling and Coulomb correlations in support of the QSL state with multiple degenerated magnetic configurations.

Results and discussion

DC susceptibility

As described in the Methods, we have performed single crystal X-ray diffraction refinement, which indicates that our single crystal forms the $R\bar{3}m$ (No. 166) symmetry with stoichiometry and the lattice parameters $a = 4.3468(7)$ Å and $c = 24.945(8)$ Å, illustrated in Fig. 1a. The Nd-Nd distance in the ab plane is 4.3468(8) Å (see Fig. 1b). The flat surface shown in the inset of Fig. 1c corresponds to the ab plane as reflected by the X-ray diffraction pattern in Fig. 1c. The formation of the trigonal symmetry ($R\bar{3}m$) in $CsNdSe_2$ implies a perfect triangular lattice. Compared to $CsYbSe_2$, both lattice parameters a and c for $CsNdSe_2$ are larger due to the larger Nd ionic radius than Yb[45]. Figure 2a–c presents the temperature dependence of the inverse DC susceptibility for a $CsNdSe_2$ single crystal along three directions: $H_{DC}||a$ (Fig. 2a), $H_{DC}||b$ (Fig. 2b), $H_{DC}||c$ (Fig. 2c). For clarity, data shown in Fig. 2a–c is obtained from the field-cooling (FC) mode. Measurements obtained from the zero-field-cooling (ZFC) mode reveal undistinguishable results from that in the FC mode. At room temperature, there is little anisotropy in $\chi^{-1}(T)$ at 0.1 T, which exhibits linear behavior above 250 K for all three directions. The Curie-Weiss expression, $\chi(T) = \chi_0 + C/(T - \theta_{CW})$, is used to fit the data between 250 K and 350 K, where χ_0 and C are constants and θ_{CW} is the Curie-Weiss temperature. The fitting parameters are shown in Table 1. The effective moment is 3.67–4.00 μ_B, close to 3.87 μ_B for free Nd^{3+} ion with $S = 3/2$. The negative Curie-Weiss temperature ($\theta_{CW} < 0$) indicates AFM interaction between Nd^{3+} ions.

At low temperatures ($T < 100$ K), the temperature dependence of the inverse magnetic susceptibility deviates from the high-temperature (HT) Curie-Weiss behavior with increased anisotropy between the in-plane and out-of-plane. Similar behavior is observed in $AYbCh_2$ compounds[22,34]. This was explained by Li et al.[12] for Yb^{3+}. For Nd^{3+}, SOC leads to the total angular momentum $J_{total} = 9/2$ with orbital angular momentum $L = 3$ and total $S = 3/2$. The total ten states $(2J + 1)$ are degenerate at high temperatures. The CEF further splits to ten $J_{total} = 9/2$ states into five pairs of Kramer's doublets[12]. At low temperatures, the ground state is well separated from the excited states[12]. Thus, the effective spin-1/2 ground state may be formed as illustrated in Fig. 2j. At low temperatures, the Curie-Weiss expression is also used to fit the data between 2 K and 4 K. The related fitting parameters are shown in Table 1. To check χ_0 for the low-temperature region, we measure the isothermal magnetization up to 14 T along the three directions, which is shown in Fig. 2d–f. Note that the magnetization along either direction increases nonlinearly with H_{DC}. However, no hysteresis has been found with all field directions, suggesting that there is negligible ferromagnetic interaction. The low-field nonlinearity can be attributed to the Zeeman effect with $E_z = g\mu_B H$ resulting in the energy level change (see Fig. 2j), where g is the Landé factor, μ_B is Bohr magneton. The linear fitting of $M(H_{DC})$ in high magnetic fields allows us to obtain the slope in three directions: $\chi_0^a = 0.024\mu_B T^{-1}, \chi_0^{b^*} = 0.025\mu_B T^{-1}$, and $\chi_0^c = 0.028\mu_B T^{-1}$. These values are consistent with our LT Curie-Weiss fitting parameters.

After the subtraction of χ_0, the temperature dependence of $1/(\chi - \chi_0)$ presents linear behavior at low temperatures (LT), as shown in Fig. 2g–i. The LT effective moment is ~ $2\mu_B$, which is lower than the Nd^{3+} moment at the high-temperature region due to the effects of SOC and CEF, which is illustrated in Fig. 2j. The LT effective moment corresponds to an effective spin-1/2 state, similar to that in Nd_2O_3[46] and $Nd_2Zr_2O_7$[47]. Compared to the HT case, the θ_{CW} value is much smaller at LT in all three directions, implying much weaker AFM interaction. Interestingly, $\theta_{CW}(H_{DC}||a)$ is almost the same as $\theta_{CW}(H_{DC}||b^*)$, while $\theta_{CW}(H_{DC}||c)$ is much smaller. This indicates that magnetic interaction is stronger in the ab plane than that in the c direction at low temperatures.

Magnetic interactions

Considering the XXZ model for $R\bar{3}m$ space group[33,48], we adapt the general spin Hamiltonian that includes a nearest neighbor exchange interaction and

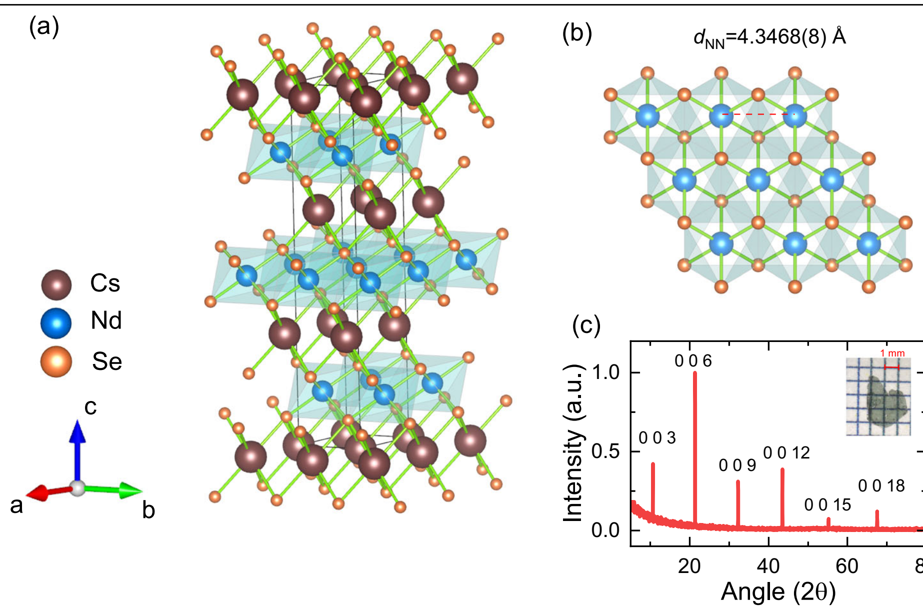

Fig. 1 | $CsNdSe_2$ structural characterization. **a** Crystal structure of $CsNdSe_2$ ($R\bar{3}m$); **b** Nd triangular layer (ab plane); **c** X-ray diffraction pattern of a $CsNdSe_2$ single crystal. Inset: Picture of a $CsNdSe_2$ single crystal.

Zeeman coupling to the external field:

$$H=\sum_{<ij>}\left\{J_{\perp}\left(S_i^xS_j^x+S_i^yS_j^y\right)+J_zS_i^zS_j^z+\frac{1}{2}J_{\Delta}\left(e^{i\phi_{ij}}S_i^-S_j^-+e^{-i\phi_{ij}}S_i^+S_j^+\right)\right.$$
$$\left.+\frac{1}{2i}J_{yz}\left[e^{i\phi_{ij}}\left(S_i^zS_j^++S_i^+S_j^z\right)-e^{-i\phi_{ij}}\left(S_i^zS_j^-+S_i^-S_j^z\right)\right]\right\}$$
$$-\mu_0\mu_B\sum_i\left[g_{\perp}\left(H_xS_i^x+H_yS_i^y\right)+g_{||}H_zS_i^z\right],$$
$$\phi_{ij}=\begin{cases}0, & \vec{R}_i-\vec{R}_j=(\pm1,0),\\ \frac{2\pi}{3}, & \vec{R}_i-\vec{R}_j=\pm\left(-\frac{1}{2},\frac{\sqrt{3}}{2}\right),\\ -\frac{2\pi}{3}, & \vec{R}_i-\vec{R}_j=\pm\left(-\frac{1}{2},-\frac{\sqrt{3}}{2}\right),\end{cases} \tag{1}$$

with $S_l^{\pm}=S_l^x\pm S_l^y$. Here, $J_{\perp}=1/2(J_a+J_b), J_{\Delta}=1/2(J_a-J_b), J_z=J_c$. From this spin Hamiltonian, we can estimate exchange interactions J_a and J_c through the following relationship:

$$\theta_{\rm cw}^a=-(3/2)J_a/k_{\rm B} \tag{2}$$

$$\theta_{\rm cw}^c=-(3/2)J_c/k_{\rm B}. \tag{3}$$

Using $\theta_{\rm cw}^a$ and $\theta_{\rm cw}^c$ in Table 1, we obtain the nearest neighbor anisotropic spin exchange parameters: in-plane component $J_a/k_{\rm B}=1.42$ K and out-of-plane component $J_c/k_{\rm B}=0.44$ K. The anisotropy ratio J_a/J_c is slightly higher than that in $NaYbSe_2$[32] and $CsYbSe_2$[34]. This can be explained by large Nd and Cs ionic radii, inducing higher anisotropy.

Ground state

Since the DC magnetic susceptibility shows no sign of any magnetic transition down to 1.8 K, we further measure the AC susceptibility down to 0.04 K to investigate the magnetic properties of the ground state. Figure 3a presents the temperature dependence of the real component of the AC susceptibility χ' at the zero DC field in three directions ($H_{\rm AC}||\ a$, $H_{\rm AC}||\ b^*$, and $H_{\rm AC}||\ c$). A broad hump centered ~ 0.4 K in χ_a' and χ_{b^*}' but ~ 0.3 K in χ_c' is revealed. We can use the Padé approximation to estimate the exchange J[33,49]

$$\chi'(T)\propto\frac{N_{\rm A}\mu_0g^2\mu_{\rm B}^2}{4k_{\rm B}T}\frac{1+b_1x+\cdots+b_6x^7}{1+c_1x+\cdots+c_7x^7}. \tag{4}$$

where $x=J/(4k_{\rm B}T)$, $N_{\rm A}$ is Avogadro constant, and the coefficients b_i and c_i are based on a spin-1/2 triangular-lattice AFM model[50]. The fittings are shown in the inset of Fig. 3a with $J_a/k_{\rm B}=1.32$ K and $J_c/k_{\rm B}=0.55$ K. Both J_a and J_c are close to our estimations from $\theta_{\rm CW}$. According to Ref. [48], the broad hump of the magnetic susceptibility is expected at $T<J/k_{\rm B}$ in a quasi-2D magnet. As shown in Fig. 3b, the broad hump remains at the same temperature between 79 Hz and 991 Hz. This indicates that the increased activated energy does not affect the temperature for the broad hump, excluding scenarios like short-range AFM correlation, spin glass, or spin ice transition[51].

AC susceptibility and $H-T$ phase diagram

To gain insight into magnetic interaction, we measure the AC susceptibility down to 0.04 K by applying DC magnetic field $H_{\rm DC}||\ a$, $H_{\rm DC}||b^*$, and $H_{\rm DC}||\ c$. As shown in Fig. 4a, the temperature dependence of χ' remains a broad hump up to $H_{\rm DC}=0.04$ T. Upon the increase of the DC field, a small peak gradually emerges above 0.11 T at $H_{\rm DC}||\ a$. This peak enhances and shifts to higher temperatures until the merge with the broad hump at $T=0.3$ K and $H_{\rm DC}=0.53$ T. With the further increase of the applied DC field, the peak shifts to lower temperatures until vanishing. When the DC magnetic field is applied parallel to b^*, the broad hump becomes sharper with the center shifts to lower temperatures. The feature also occurs when the DC magnetic field is applied to the c axis, as shown in Fig. 4c.

The characteristic temperature at each applied DC field is plotted in Fig. 4d–f. The green circles represent the broad hump at low fields and the violet squares denote temperatures at sharp peaks. The general trend is that the DC magnetic field forces AFM magnetic alignment, resulting in a long-range AFM ordering ($T_{\rm N}$) with the highest ordering temperature at 0.3 K. The dome-like H-$T_{\rm N}$ diagram is typical for quantum magnetic systems, as the result of competing field-enhanced spin interaction and the quantum effects of exchange randomness[32,52].

We also measure the DC field dependence of the AC susceptibility at 0.04 K to check the field-induced states. Figure 5a, b present the magnetic field dependence of the real component of the AC susceptibility at $H_{\rm DC}||\ a$ and $H_{\rm DC}||\ c$, respectively. Four anomalies for $H_{\rm DC}||\ a$ and three for $H_{\rm DC}||\ c$ are observed as indicated by arrows in Fig. 5. The first upturn is observed at 0.05 T for $H_{\rm DC}||\ a$ and 0.09 T for $H_{\rm DC}||\ c$, which may be related to the Zeeman effect that splits each state to two levels (see Fig. 2j). The in-plane shoulder-like anomalies are similar to previously reported dM/dH in $AYbSe_2$[22,32,34], suggesting field-induced spin reorientation in $CsNdSe_2$. The potential spin structures with applied magnetic fields are illustrated in Fig. 5. When the DC magnetic field is applied along the a axis, an oblique 120° state is induced. With the further increase of $H_{\rm DC}>0.5$ T, χ_a' reaches a plateau.

By calculating the magnetization through integrating χ' with the DC magnetic field in two directions as shown in Fig. 5c–d, respectively, we note that the plateau corresponds to the magnetization of 30% $M_{a,\rm sat}$ and 34% $M_{c,\rm sat}$, where $M_{a,\rm sat}$ and $M_{c,\rm sat}$ are saturation values for the a and c directions. This suggests the up-up-down magnetic configuration as observed in other quantum magnets[22,33]. Such a magnetic configuration is also predicted in the quantum phase diagram of the triangular-lattice XXZ model in the magnetic field for $J_{\perp}/J_z<\sim1.4$[53]. However, our low-temperature magnetization suggests $J_a/J_c>3$ for $CsNdSe_2$, which is beyond the phase diagram presented in ref. 53. With further increasing $H_{\rm DC}$, χ_a' shows another plateau around 1 T, which corresponds to $1/2M_{a,\rm sat}$ (see the corresponding vertical dashed line). Such a 1/2 plateau state was theoretically and experimentally studied in triangular lattice systems, which occurs when the interaction with the next nearest neighbors is not negligible[31,54,55]. Because of this, three aligned spins in one sublattice are anti-aligned with the spin in the next sublattice, forming the so-called up-up-up-down (uuud) configuration. Note that the 1/2 plateau is absent in χ_c', as the spin interaction with the next nearest neighbors is negligible along the c direction.

First-principles calculations

To find out possible magnetic states, we construct supercells that host several long-range ordered magnetic configurations and evaluate their total energies at zero magnetic fields. The magnetic configurations are illustrated in Fig. 6, including stripe (a), up-up-up-down (b), 120° noncollinear (c), two in-equivalent antiferromagnetic spins in a $2\times2\times1$ supercell (d), $2\times\sqrt{3}\times1$ supercell (e), an up-up-down (f), and ferromagnetic (FM) spin configuration. With spin–orbit coupling, all spins favor in-plane orientations, yielding in-plane magnetic anisotropy for all considered spin configurations. The energies per formula unit (f.u.) are shown in the histogram [see Fig. 6g], referenced to the total energy of the stripe spin configuration (case (a)), are shown in Fig. 6g, denoted as b-a, c-a, d-a, e-a, f-a, and FM-a. Here, FM represents ferromagnetic spin configuration (not shown). The stripy configuration (case(a)) has the lowest total energy among the seven considered spin configurations, which is further set as a reference. The calculated spin moment on Nd is $3\mu_{\rm B}$ and the orbital moment is $-1.5\mu_{\rm B}$, yielding a net moment of $1.5\mu_{\rm B}$ on each Nd. This is close to the measured $\mu_{\rm eff}$ ($\sim2\mu_{\rm B}$) at low temperatures. The two antiferromagnetic spin configurations (d–e), which give zero net magnetization, possess competing total energies (less than 5 meV f.u.$^{-1}$) to the stripe configuration (see Fig. 6). The discovery of multiple energy-competing spin configurations indicates strong spin fluctuation and the disordered spin-liquid state could be formed. The total energy of the up-up-down spin configuration is modest (36 meV f.u.$^{-1}$), which can be achieved under an applied magnetic field, yielding a 1/3 magnetization that is consistent with our experimental observation.

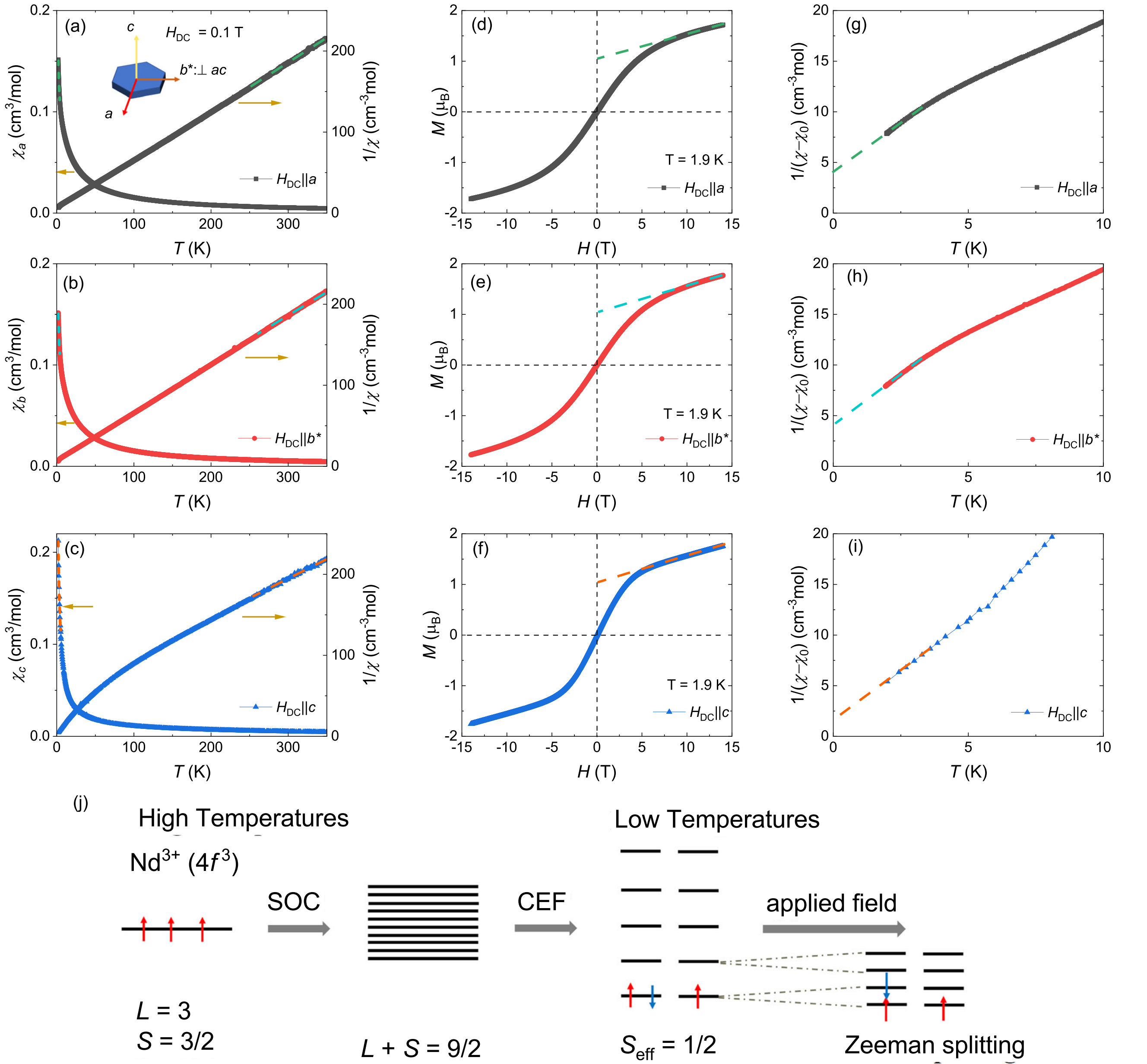

Fig. 2 | Magnetization results of $CsNdSe_2$. **a–c** Temperature dependence of the inverse DC susceptibility at $H_{DC} = 0.1$ T for the $CsNdSe_2$ single crystal with $H_{DC}\|$ *a*, $H_{DC}\|b^*$, and $H_{DC}\|$ *c*. Dash lines show the fit to the Curie-Weiss law ($\chi(T) = \chi_0 + C/(T-\theta_{CW})$) at high temperatures (HT) (250 − 350 K) and low temperatures (LT) (2−4 K). The fitting parameters are shown in Table 1. **d–f** Isothermal magnetization at 1.9 K with $H_{DC}\|$ *a*, $H_{DC}\|b^*$, and $H_{DC}\|$ *c*. The dash lines guide the linear relation at the high magnetic field area. **g–i** Temperature dependence of $1/(\chi$-$\chi_0)$ below 10 K. The dash lines present the linear behavior below 4 K. **j** Illustration of the Nd^{3+} moment due to the effects of SOC and CEF.

Table 1 | Curie-Weiss fitting results

HT (250–350 K)	$H\|$ a	$H\|b^*$	$H\|$ c
$\mu_{eff}[\mu_B]$	4.00	3.67	3.99
θ_{CW}[K]	−30.9	−10.6	−81.1
$\chi_0[\mu_B\ T^{-1}]$	−0.0013	−0.0002	0.0038
LT (2–4 K)	**$H\|$ a**	**$H\|b^*$**	**$H\|$ c**
$\mu_{eff}[\mu_B]$	2.00	2.01	1.97
θ_{CW}[K]	−2.14	−2.19	-0.66
$\chi_0[\mu_B\ T^{-1}]$	0.042	0.044	0.049

The effective magnetic moment (μ_{eff}) and Curie-Weiss temperature (θ_{CW}) were obtained from the fit at high temperatures (HT) (250−350 K) and low temperatures (LT) (2 K to 4 K).

Surprisingly, the up-up-up-down (case (b)) spin configuration possesses a lower total energy than the up-up-down case, which needs to be further investigated. For the ferromagnetic state and the 120° noncollinear spin configuration, greater total energies (>46 meV f.u.$^{-1}$) are observed, indicating a strong antiferromagnetic coupling that could go beyond the next nearest neighbor[56]. In fact, the spin state in $CsNdSe_2$ is reflected from in-plane shoulder-like anomalies under a DC magnetic field (see Fig. 5). The calculated total energy of 120° noncollinear spin configurations in $CsNdSe_2$ may indicate that this state could be achieved.

The in-plane $H-T$ phase diagram of $CsNdSe_2$ (Fig. 4d–f) is close to that in $CsYbSe_2$[34,38]. One unique feature of $CsNdSe_2$ is that a much weaker in-plane field ($H < 0.11$ T) could induce long-range ordering in $CsNdSe_2$. On the other hand, the out-of-plane field could also induce clear anomalies

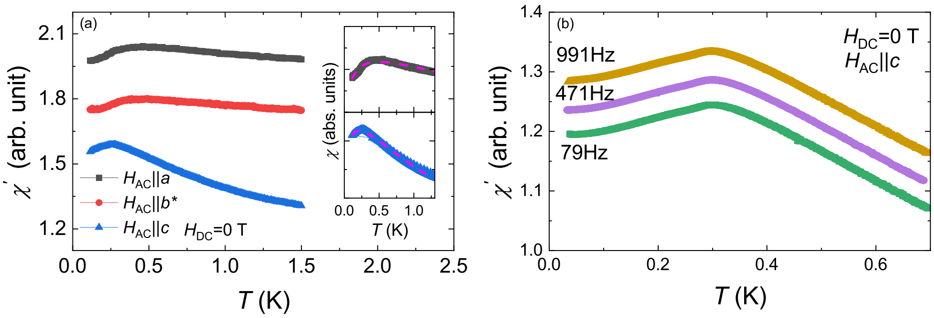

Fig. 3 | AC susceptibility of $CsNdSe_2$ at zero DC field. **a** Temperature dependence of the real component of the AC susceptibility at zero DC field. Inset: the Padé approximation fitting for spin-1/2 triangular-lattice antiferromagnet. **b** Temperature dependence of the real component of the AC susceptibility under different frequencies. The offset has been set for each data for the visual guide.

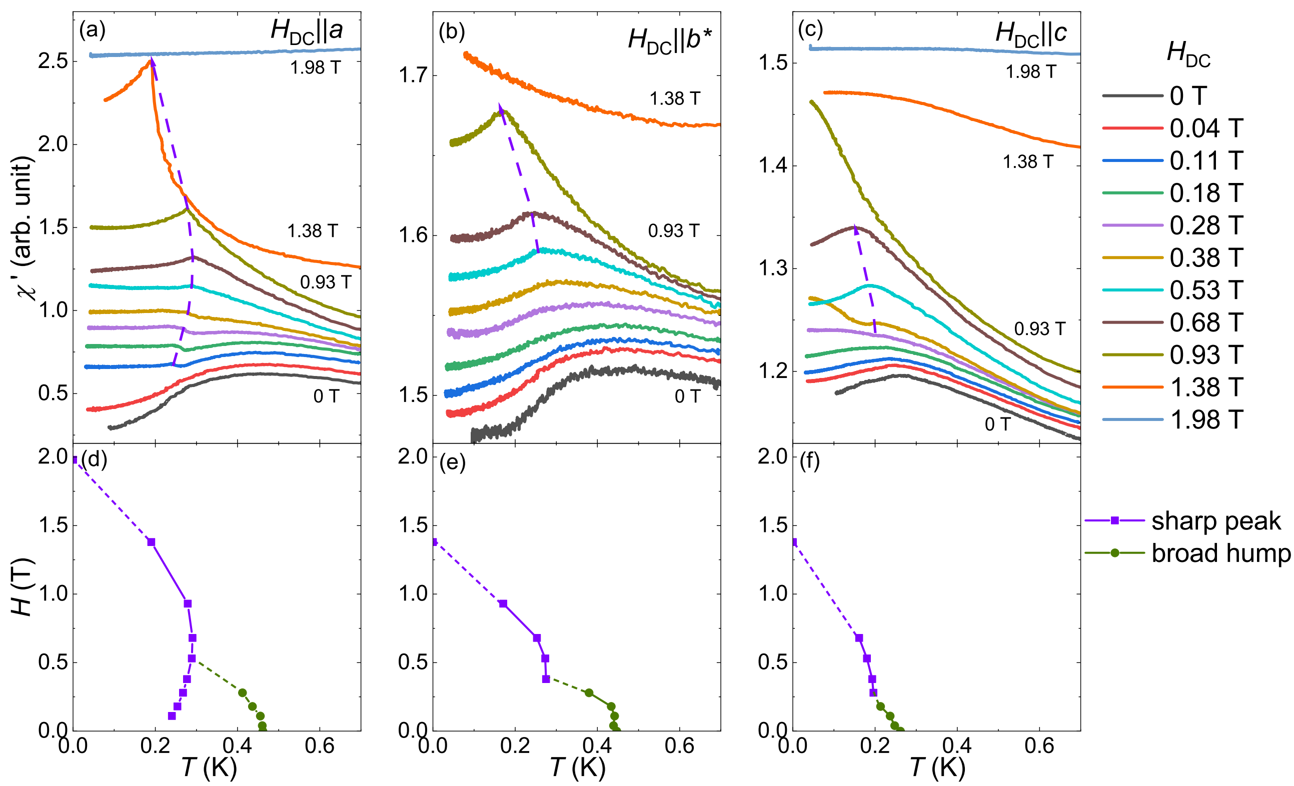

Fig. 4 | Field-induced LROs in $CsNdSe_2$. **a–c** Temperature dependence of the real component of the AC susceptibility under DC magnetic field from 0 T to 1.98 T at $H_{DC}||\ a$, $H_{DC}||\ b^*$, and $H_{DC}||\ c$. The offset has been set for each data for the visual guide. **d–f** $H-T$ phase diagram at $H_{DC}||\ a$, $H_{DC}||\ b^*$, and $H_{DC}||\ c$.

in DC field dependence of χ'. Compared to Ce or Yb compounds, this feature is closer to transition metal triangular-lattice antiferromagnet $Ba_3CoSb_2O_9$[57]. Based on our AC and DC magnetization, $CsNdSe_2$ is an effective spin-1/2 quasi-2D material with anisotropic exchange. Compared to $AYbCh_2$, $CsNdSe_2$ only needs a 2–3 T magnetic field to reach excited magnetic states. Our work extends the quantum magnetism investigation to quasi-2D materials with Nd triangular lattice and sheds light to further investigate the magnetism with effective spin-1/2 Nd triangular-lattice antiferromagnets.

Conclusion

In conclusion, we successfully synthesize $CsNdSe_2$ single crystals with the triangular lattice and measure the DC and AC susceptibility along three crystal orientations, $H||\ a$, $H||\ b^*$, and $H||\ c$. Through the DC susceptibility, an effective spin-1/2 of Nd state with AFM interactions has been found at the low-temperature region. There is no evidence for any long-range magnetic ordering down to 0.04 K. A broad hump appears in the AC susceptibility below 0.5 K. Anisotropic in-plane interaction $J_a/k_B = 1.42$ K and out-of-plane interaction $J_c/k_B = 0.44$ K have been found by fitting experimental data to the XXZ model. The low-temperature AC susceptibility under DC magnetic fields reveals the field-induced long-range antiferromagnetic ordering in $CsNdSe_2$. These results suggest the anisotropic magnetism in quasi-2D $CsNdSe_2$, which may be close to the boundary of the QSL state and ordered state.

Methods

Materials and structural characterization

Millimeter-sized (inset of Fig. 1c) $CsNdSe_2$ single crystals are synthesized by the CsCl salt flux method[20]. X-ray diffraction is performed by Rigaku MiniFlex 600 diffractometer with Cu $K_{\alpha1}$ radiation ($\lambda = 1.5406$ Å). The crystal structure of $CsNdSe_2$ is shown in Fig. 1a, forming a $R\bar{3}m$ symmetry. As demonstrated in Fig. 1b, the shortest Nd-Nd distance is 4.3468(8) Å within the *ab* plane. The interlayer distance of Nd triangular layers is 8.315(2) Å. The X-ray diffraction pattern of a flat surface is shown in Fig. 1c. The sharp (00l) peaks suggest the good quality of our single crystals (l = integer).

Magnetic susceptibility measurements

The DC magnetization is measured using a Quantum Design (QD) DynaCool with Vibrating Sample Magnetometer (VSM) option up to

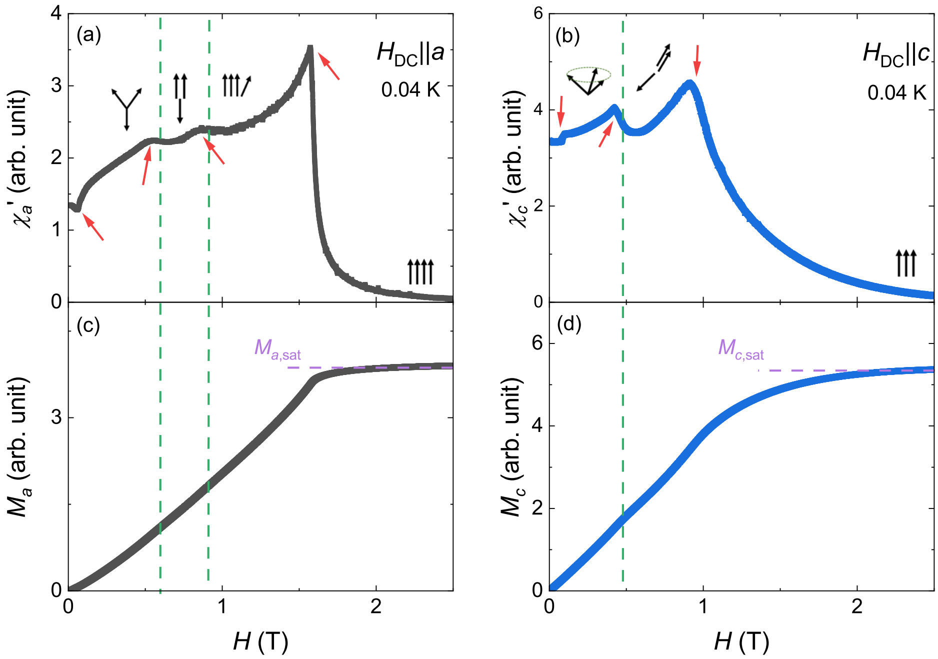

Fig. 5 | Spin states under DC magnetic fields in $CsNdSe_2$. a, b DC magnetic field dependence of the real component of the AC susceptibility at $H_{DC}||\ a$, and $H_{DC}||\ c$ up to 2.5 T. The green dash lines indicate the first peak position through the field scan. **c, d** DC magnetic field dependence of moment.

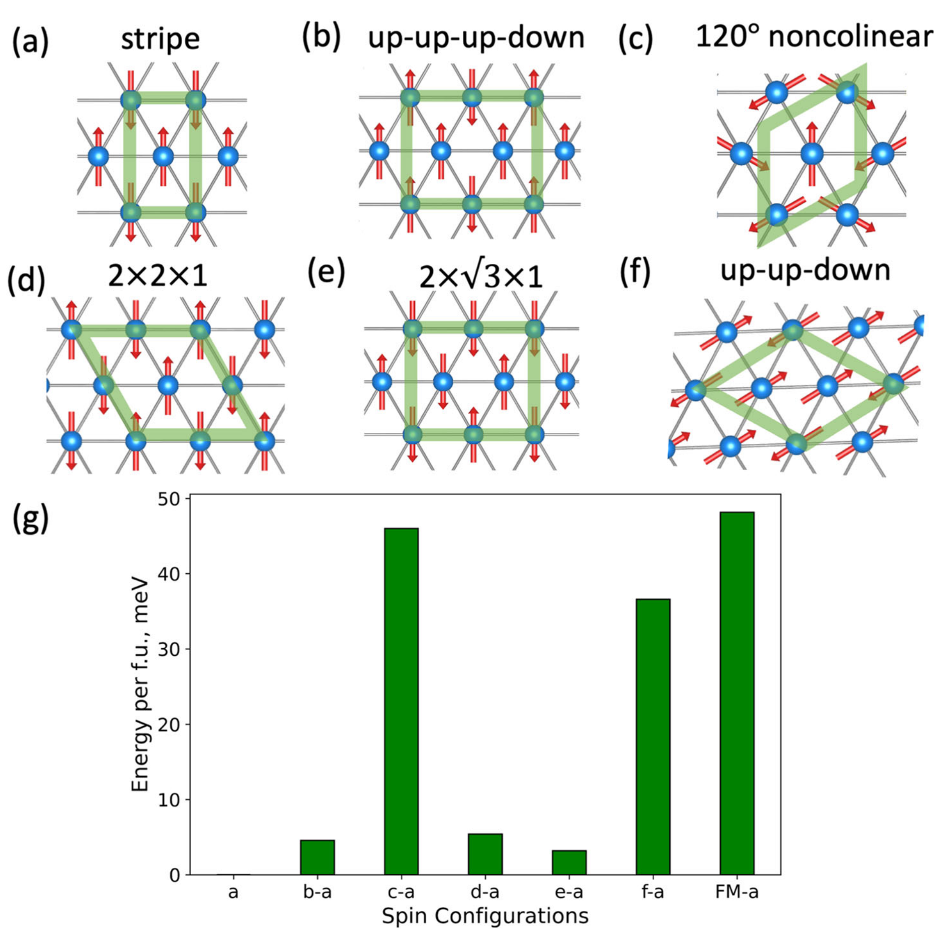

Fig. 6 | Spin configurations with relative energies. a–f Multiple spin configurations investigated for $CsNdSe_2$. Red arrows indicate the spin directions, and the thick green boundaries denote the unit cell boundary to simulate the corresponding spin configurations. **g** Relative energies (per formula unit) for different spin configurations referenced to the total energy of the strip spin configuration, including the ferromagnetic (FM) case.

14 T and magnetic property measurement system (MPMS) up to 7 T. AC susceptibility is measured using an apparatus at SCM1 of National High Magnetic Field Laboratory (NHMFL) down to 0.04 K. Data shown in this manuscript are obtained with $H_{AC} \sim 2$ Oe. An empirical background of the coil is removed for the integration of the AC susceptibility.

First-principles calculation methods

Density functional theory (DFT) calculations were performed using projector augmented wave (PAW)[58] potentials as implemented in the Vienna Ab-initio Simulation Package[59,60]. A 500-eV kinetic energy cutoff has been chosen for plane wave expansion. The PAW pseudopotentials correspond to the valence-electron configuration $6s^1 5p^6 5s^2$ for Cs, $4f^4 5p^6 5s^2 6s^2$ for Nd, and $4s^2 4p^4$ for Se. The exchange correlation is treated within the generalized gradient approximation, parameterized by Perdew, Burke, and Ernzerhof [61]. The Coulomb correlations within the 4*f* shells of Nd were described using the spherically averaged GGA + U method[62], with $U_{\mathrm{eff}} = 6$ eV. Spin polarization was included in all calculations and spin–orbit coupling was included, which allows for the assessment of the magnetic anisotropy. The lattice constants of the unit cell of $CsNdSe_2$ were fixed to the experimental values, with $a = 4.3468$ Å and $c = 24.9450$ Å. The Brillouin Zone (BZ) integration for the primitive cell is performed using a Γ-centered $6 \times 6 \times 1$ k-point mesh. The internal atomic positions were relaxed until the maximum force on each atom was less than 10 meV Å^{-1}. The total energies were converged to 10^{-6} eV.

Data availability

The data that support the findings of this study are available from the corresponding author upon reasonable request.

Received: 9 August 2023; Accepted: 22 March 2024;
Published online: 04 April 2024

References

1. Anderson, P. Resonating valence bonds: a new kind of insulator? *Mater. Res. Bull.* **8**, 153–160 (1973).
2. Balents, L. Spin liquids in frustrated magnets. *Nature* **464**, 199–208 (2010).
3. Zhou, Y., Kanoda, K. & Ng, T. Quantum spin liquid states. *Rev. Mod. Phys.* **89**, 025003 (2017).
4. Kohno, M., Starykh, O. A. & Balents, L. Spinons and triplons in spatially anisotropic frustrated antiferromagnets. *Nat. Phys.* **3**, 790–795 (2007).
5. Kitaev, A. Y. Fault-tolerant quantum computation by anyons. *Ann. Phys.* **303**, 2–30 (2003).
6. Isono, T., Terashima, T., Miyagawa, K., Kanoda, K. & Uji, S. Quantum criticality in an organic spin-liquid insulator κ-$(BEDT\text{-}TTF)_2Cu_2(CN)_3$. *Nat. Commun.* **7**, 1–5 (2016).
7. Itou, T., Oyamada, A., Maegawa, S., Tamura, M. & Kato, R. Quantum spin liquid in the spin-1/2 triangular antiferromagnet $EtMe_2Sb[Pd(dmit)_2]_2$. *Phys. Rev. B* **77**, 104413 (2008).
8. Clark, L. et al. Two-dimensional spin liquid behaviour in the triangular-honeycomb antiferromagnet $TbInO_3$. *Nat. Phys.* **15**, 262–268 (2019).
9. Mustonen, O. et al. Spin-liquid-like state in a spin-1/2 square-lattice antiferromagnet perovskite induced by d^{10} - d^0 cation mixing. *Nat. Commun.* **9**, 1085 (2018).
10. Clark, L. et al. From spin glass to quantum spin liquid ground states in molybdate pyrochlores. *Phys. Rev. Lett.* **113**, 117201 (2014).
11. Coldea, R., Tennant, D. A., Tsvelik, A. M. & Tylczynski, Z. Experimental realization of a 2D fractional quantum spin liquid. *Phys. Rev. Lett.* **86**, 1335 (2001).
12. Li, Y., Wang, X. & Chen, G. Anisotropic spin model of strong spin-orbit-coupled triangular antiferromagnets. *Phys. Rev. B* **94**, 035107 (2016).
13. Xing, J. et al. Néel-type antiferromagnetic order and magnetic field-temperature phase diagram in the spin-1/2 rare-earth honeycomb compound $YbCl_3$. *Phys. Rev. B* **102**, 014427 (2020).
14. Li, Y. et al. Gapless quantum spin liquid ground state in the two-dimensional spin-1/2 triangular antiferromagnet $YbMgGaO_4$. *Sci. Rep.* **5**, 16419 (2015).
15. Li, Y. et al. Rare-earth triangular lattice spin liquid: a single-crystal study of $YbMgGaO_4$. *Phys. Rev. Lett.* **115**, 167203 (2015).
16. Li, Y. $YbMgGaO_4$: a triangular-lattice quantum spin liquid candidate. *Adv. Quant. Technol.* **2**, 1900089 (2019).
17. Paddison, J. A. M. et al. Continuous excitations of the triangular-lattice quantum spin liquid $YbMgGaO_4$. *Nat. Phys.* **13**, 117 (2017).
18. Zhu, Z., Maksimov, P. A., White, S. R. & Chernyshev, A. L. Disorder-induced mimicry of a spin liquid in $YbMgGaO_4$. *Phys. Rev. Lett.* **119**, 157201 (2017).
19. Liu, W. et al. Rare-earth chalcogenides: a large family of triangular lattice spin liquid candidates. *Chin. Phys. Lett.* **35**, 117501 (2018).
20. Xing, J. et al. Crystal synthesis and frustrated magnetism in triangular lattice $CsRESe_2$ (RE = La-Lu): quantum spin liquid candidates $CsCeSe_2$ and $CsYbSe_2$. *ACS Mater. Lett.* **2**, 71–75 (2019).
21. Bordelon, M. M. et al. Field-tunable quantum disordered ground state in the triangular-lattice antiferromagnet $NaYbO_2$. *Nat. Phys.* **15**, 1058–1064 (2019).
22. Xing, J., Sanjeewa, L. D., May, A. F. & Sefat, A. S. Synthesis and anisotropic magnetism in quantum spin liquid candidates $AYbSe_2$ (*A*= K and Rb). *APL Mater.* **9**, 111104 (2021).
23. Ma, J. Spins don't align here. *Nat. Phys.* **19**, 922–923 (2023).
24. Baenitz, M. et al. $NaYbS_2$: a planar spin-1/2 triangular-lattice magnet and putative spin liquid. *Phys. Rev. B* **98**, 220409 (2018).
25. Bordelon, M. M. et al. Spin excitations in the frustrated triangular lattice antiferromagnet $NaYbO_2$. *Phys. Rev. B* **101**, 224427 (2020).
26. Zhang, Z. et al. Crystalline electric field excitations in the quantum spin liquid candidate $NaYbSe_2$. *Phys. Rev. B* **103**, 035144 (2021).
27. Sichelschmidt, J. et al. Effective Spin-1/2 Moments on a Yb^{3+} Triangular Lattice: An ESR Study. *JPS Conf. Proc.* **30**, 011096 (2020).
28. Guo, J. et al. Magnetic-field and composition tuned antiferromagnetic instability in the quantum spin-liquid candidate $NaYbO_2$. *Phys. Rev. Mater.* **4**, 064410 (2020).
29. Zhang, Z. et al. Effective magnetic Hamiltonian at finite temperatures for rare-earth chalcogenides. *Phys. Rev. B* **103**, 184419 (2021).
30. Schmidt, B., Sichelschmidt, J., Ranjith, K. M., Doert, T. & Baenitz, M. Yb delafossites: unique exchange frustration of 4*f* spin-$\frac{1}{2}$ moments on a perfect triangular lattice. *Phys. Rev. B* **103**, 214445 (2021).
31. Wu, J. Magnetic field effects on the quantum spin liquid behaviors of $NaYbS_2$. *Quant. Front.* **1**, 13 (2022).
32. Ranjith, K. M. et al. Field-induced instability of the quantum spin liquid ground state in the $J_{\mathrm{eff}} = \frac{1}{2}$ triangular-lattice compound $NaYbO_2$. *Phys. Rev. B* **99**, 180401 (2019).
33. Ranjith, K. M. et al. Anisotropic field-induced ordering in the triangular-lattice quantum spin liquid $NaYbSe_2$. *Phys. Rev. B* **100**, 224417 (2019).
34. Xing, J. et al. Field-induced magnetic transition and spin fluctuations in the quantum spin-liquid candidate $CsYbSe_2$. *Phys. Rev. B* **100**, 220407 (2019).
35. Ferreira, T., Xing, J., Sanjeewa, L. D. & Sefat, A. S. Frustrated magnetism in triangular lattice $TlYbS_2$ crystals grown via molten flux. *Front. Chem.* **8**, 127 (2020).
36. Ranjith, K. M. and Schlender, Ph. and Doert, Th. and Baenitz, M. Magnetic properties of an effective spin-1/2 triangualr lattcie compound $LiYbS_2$. *JPS Conf. Proc.* **30**, 011094 (2020).
37. Dai, P.-L. et al. Spinon fermi surface spin liquid in a triangular lattice antiferromagnet $NaYbSe_2$. *Phys. Rev. X* **11**, 021044 (2021).
38. Xie, T. et al. Complete field-induced spectral response of the spin-1/2 triangular-lattice antiferromagnet $CsYbSe_2$. *npj Quant. Mater.* **8**, 48 (2023).
39. Scheie, A. et al. Proximate spin liquid and fractionalization in the triangular antiferromagnet $KYbSe_2$. *Nat. Phys.* **20**, 74–81 (2024).
40. Kulbakov, A. A. et al. Stripe-yz magnetic order in the triangular-lattice antiferromagnet $KCeS_2$. *J. Phys. Condens. Matter* **33**, 425802 (2021).
41. Sanjeewa, L. D., Xing, J., Taddei, K. M. & Sefat, A. S. Synthesis, crystal structure and magnetic properties of $KLnSe_2$ (Ln= La, Ce, Pr, Nd) structures: a family of 2D triangular lattice frustrated magnets. *J. Solid State Chem.* **308**, 122917 (2022).
42. Bordelon, M. M. et al. Magnetic properties and signatures of moment ordering in the triangular lattice antiferromagnet $KCeO_2$. *Phys. Rev. B* **104**, 094421 (2021).

43. Xing, J. et al. Synthesis, magnetization, and heat capacity of triangular lattice materials $NaErSe_2$ and $KErSe_2$. *Phys. Rev. Mater.* **3**, 114413 (2019).
44. Xing, J. et al. Stripe antiferromagnetic ground state of the ideal triangular lattice compound $KErSe_2$. *Phys. Rev. B* **103**, 144413 (2021).
45. Jensen, J. & Mackintosh, A. R. *Rare Earth Magnetism* (Clarendon Press Oxford, 1991).
46. Sala, G. et al. Physical properties of the trigonal binary compound Nd_2O_3. *Phys. Rev. Mater.* **2**, 114407 (2018).
47. Xu, J. et al. Magnetic structure and crystal-field states of the pyrochlore antiferromagnet $Nd_2Zr_2O_7$. *Phys. Rev. B* **92**, 224430 (2015).
48. Schmidt, B. & Thalmeier, P. Frustrated two dimensional quantum magnets. *Phys. Rep.* **703**, 1–59 (2017).
49. Elstner, N., Singh, R. P. & Young, A. P. Finite temperature properties of the spin-1/2 Heisenberg antiferromagnet on the triangular lattice. *Phys. Rev. Lett.* **71**, 1629 (1993).
50. Tamura, M. & Kato, R. Magnetic susceptibility of β'-[Pd(dmit)$_2$] salts (dmit= 1,3-dithiol-2-thione-4,5-dithiolate, C3S5): evidence for frustration in spin-1/2 Heisenberg antiferromagnets on a triangular lattice. *J. Phys. Condens. Matter* **14**, L729 (2002).
51. Topping, C. V. & Blundell, S. J. AC susceptibility as a probe of low-frequency magnetic dynamics. *J. Phys. Condens. Matter* **31**, 013001 (2018).
52. Savary, LandBalents,L. Quantum spin liquids: a review. *Rep. Prog. Phys.* **80**, 016502 (2016).
53. Yamamoto, D., Marmorini, G. & Danshita, I. Quantum phase diagram of the triangular-lattice XXZ model in a magnetic field. *Phys. Rev. Lett.* **112**, 127203 (2014).
54. Ye, M. & Chubukov, A. V. Half-magnetization plateau in a Heisenberg antiferromagnet on a triangular lattice. *Phys. Rev. B* **96**, 140406 (2017).
55. Zheng, W., Singh, R. R. P., McKenzie, R. H. & Coldea, R. Temperature dependence of the magnetic susceptibility for triangular-lattice antiferromagnets with spatially anisotropic exchange constants. *Phys. Rev. B* **71**, 134422 (2005).
56. Kurz, P., Bihlmayer, G., Hirai, K. & Blügel, S. Three-dimensional spin structure on a two-dimensional lattice: Mn/Cu (111). *Phys. Rev. Lett.* **86**, 1106 (2001).
57. Susuki, T. et al. Magnetization process and collective excitations in the S= 1/2 triangular-lattice Heisenberg antiferromagnet $Ba_3CoSb_2O_9$. *Phys. Rev. Lett.* **110**, 267201 (2013).
58. Blöchl, P. E. Projector augmented-wave method. *Phys. Rev. B* **50**, 17953 (1994).
59. Kresse, G. & Hafner, J. Ab initio molecular dynamics for open-shell transition metals. *Phys. Rev. B* **48**, 13115 (1993).
60. Kresse, G. & Furthmüller, J. Efficient iterative schemes for ab initio total-energy calculations using a plane-wave basis set. *Phys. Rev. B* **54**, 11169 (1996).
61. Perdew, J. P., Burke, K. & Ernzerhof, M. Generalized gradient approximation made simple. *Phys. Rev. Lett.* **77**, 3865 (1996).
62. Dudarev, S. L., Botton, G. A., Savrasov, S. Y., Humphreys, C. J. & Sutton, A. P. Electron-energy-loss spectra and the structural stability of nickel oxide: an LSDA+ U study. *Phys. Rev. B* **57**, 1505 (1998).

Acknowledgements

We thank Daniel Duong for his assistance in characterizing crystals. This material is based upon work partially supported by the U.S. Department of Energy under Grant No. DE-SC0024501. Work performed at the National High Magnetic Field Laboratory is supported by National Science Foundation Cooperative agreement No. DMR-1644779 and the state of Florida. Sai Mu would like to acknowledge the Research Computing time under the Division of Information Technology at the University of South Carolina.

Author contributions

R.J. conceived and supervised the research. J.X. synthesized the sample and conducted physical property measurements with assistance from E.S.C. S.M. performed the first-principle calculations. J.X., S.M. and R.J. wrote the manuscript with contributions from all the authors.

Competing interests

The authors declare no competing interests.

Additional information

Supplementary information The online version contains supplementary material available at https://doi.org/10.1038/s43246-024-00483-7.

Correspondence and requests for materials should be addressed to Rongying Jin.

Peer review information *Communications Materials* thanks Hidekazu Tanaka, Girish Tewari, and the other, anonymous, reviewer(s) for their contribution to the peer review of this work. Primary handling editors: Toru Hirahara and Aldo Isidori. A peer review file is available.